Communication

V-Band Geodesic Generalized Luneburg Lens Antenna With High Beam Crossover Gain

O. Zetterstrom, P. Arnberg, F. V. Vidarsson, A. Algaba-Brazález, L. Manholm, M. Johansson, and O. Quevedo-Teruel

***Abstract*— Quasi-optical beamformers provide attractive properties for antenna applications at millimeter-wave (mm-wave) frequencies. Antennas implemented with these beamformers have demonstrated wide-angle switching of directive beams, making them suitable as base station antennas for future communication networks. For these applications, it is essential to ensure a high beam crossover gain to provide a robust service to end users within the steering range. Here, we propose a geodesic generalized Luneburg lens antenna operating from 57 to 67 GHz that provides increased crossover gain compared to previously reported geodesic Luneburg lens antennas. The focal curve of the generalized Luneburg lens can be displaced from the beamformer, allowing for a higher angular resolution in the placement of the feed array along the focal curve. The lens is fed with 21 ridge waveguides with an angular separation of 5.1°, thus providing beam steering in a 102° range. The peak realized gain varies from 19 to 21 dBi throughout the steering and frequency ranges and the beam crossover gain is roughly 3 dB below the peak gain. The simulations are experimentally validated.**

***Index Terms*— Generalized Luneburg lens, geodesic lens, lens antenna, multibeam antennas.**

I. Introduction

The future mobile networks (6G and beyond) are expected to partially operate at millimeter-wave (mm-wave) frequencies to provide the requested high data rates [1]. At these frequencies, high-gain antennas can be used to mitigate the effect of the high path loss. These antennas must have wide-angle beam steering and/or multibeam capabilities to provide sufficient coverage. Furthermore, fully-metallic solutions are attractive to avoid dielectric losses.

Parallel plate waveguide (PPW) quasi-optical beamformers have been used to develop cost-effective antennas at mm-wave frequencies [2]. These antennas are typically designed in several layers that are assembled together and where the beamformer, feeding network, and additional components are readily integrated. Many of the reported solutions provide multibeam capabilities and can steer the radiation by switching between different beams, where each beam is produced by different feeds displaced along the focal arc of the beamformer. Such PPW beamformer antennas based on reflectors have demonstrated directive radiation and beam steering ranges of roughly ±40° [3], [4]. Similar beam steering capabilities have also been demonstrated in antennas based on planar Rotman [5], [6] and other PPW [7], [8], [9] lenses. Wider beam coverage can be achieved with rotationally symmetric lenses, for example, cylindrical [10], [11] and Luneburg [12], [13], [14], [15], [16] lens antennas, and steering ranges up to ±75° have been demonstrated [10], [17].

In these beam-switching antennas, the beam resolution is limited by the dimensions of the feeding element, often a rectangular waveguide or an H-plane horn. The minimum width of these feeds is restricted by the cut-off frequency of the fundamental mode, which means that the feed separation is typically larger than half a wavelength. Such feed separation results in a beam-crossover gain that is typically more than 6 dB lower than the peak gain [15], [17]. As a result, end users in some directions will experience significantly reduced connectivity. To overcome the low crossover gain in PPW reflector-based beamformers, it has been proposed to interleave two stacked feed arrays [18]. This allows for accurate control of the crossover gain, but the implementation of stacked feeds in the small PPW gap is challenging. Furthermore, since the feeds share the same aperture, closely spaced beams can result in a high beam correlation and reduced radiation performance in terms of sidelobe levels and radiation efficiency [19], [20], [21], [22]. In [21] and [22], the interleaved feeds excite two different apertures (adjacent feeds excite different apertures), and as a result, the beam crossover is improved without impairing the radiation efficiency and sidelobe levels. However, two apertures are required, which results in a bulky system. Alternatively, continuous beam scanning can be achieved with feeds that are mechanically moved [23], [24]. However, such mechanical beam scanning is comparably slow and prohibits multiple simultaneous beams. To overcome the low beam crossover in rotationally symmetric lens antennas, [25], [26] proposes to focus the radiation in the near-field, thus increasing the beamwidth compared to far-field focused lens antennas. In this way, the wide steering capabilities of antennas based on rotationally symmetric lenses are maintained, however, the aperture efficiency is significantly reduced.

In this work, we propose a fully-metallic geodesic generalized Luneburg lens antenna with a high beam-crossover gain. This communication is an extension of [27], and we provide an experimental validation operating at the V-band. The high beam-crossover gain is obtained by placing the focal arc of the lens at a distance from the lens contour [28], thus allowing a higher angular resolution in the feed placement, compared to conventional Luneburg lens antennas [29]. Contrary to [25] and [26], the radiation is focused in the far-field, and thus, the high aperture efficiency of Luneburg lens antennas is maintained. The feed displacement is chosen so that the beam correlation is low, and as a result, high radiation efficiency is obtained. Furthermore, since the lens is rotationally symmetric, the wide steering capabilities of conventional Luneburg lens antennas are maintained, and the designed antenna can steer its beam in a

Manuscript received 2 December 2022; revised 20 April 2023; accepted 8 May 2023. Date of publication 9 June 2023; date of current version 6 September 2023. This work was supported by the Strategic Innovation Program Smarter Electronics System—A Joint Venture of Vinnova, Formas and the Swedish Energy Agency, through the Project High-Int under Grant 2019-02103. The work of O. Quevedo-Teruel was supported by the VR Project under call "Research Project Grant Within Natural and Engineering Sciences" under Grant 2019-03933. *(Corresponding author: O. Zetterstrom.)*

O. Zetterstrom, F. V. Vidarsson, and O. Quevedo-Teruel are with the Division of Electromagnetic Engineering and Fusion Science, KTH Royal Institute of Technology, 114 28 Stockholm, Sweden (e-mail: oskarz@kth.se).

P. Arnberg is with the Division of Microwave Engineering, SAAB, 175 41 Stockholm, Sweden.

A. Algaba-Brazález, L. Manholm, and M. Johansson are with Ericsson Research, Ericsson AB, 417 56 Gothenburg, Sweden.

Color versions of one or more figures in this communication are available at https://doi.org/10.1109/TAP.2023.3283138.

Digital Object Identifier 10.1109/TAP.2023.3283138

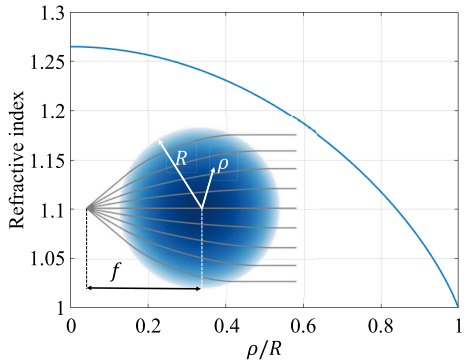

Fig. 1. Refractive index distribution in the generalized Luneburg lens with $f/R = 1.4$. The inset shows the ray paths in the lens when excited by a point source placed in the focal point.

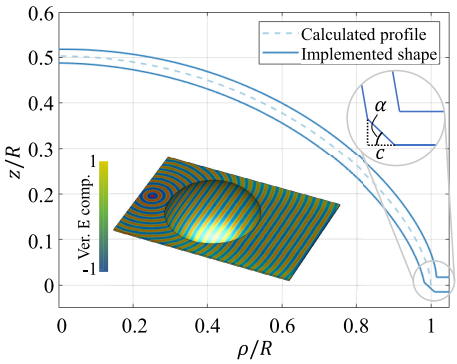

Fig. 2. Geodesic profile for a generalized Luneburg lens with $f/R = 1.4$. The inset shows the distribution of the real part of the z-component of the electric field in the PPW when excited by a point source placed in the focal point. The lens radius is $R = 25$ mm and the distance between the PPW conductors is 0.8 mm. The chamfering at $\rho = R$ has the dimensions $c = 0.7$ mm and $\alpha = 43°$.

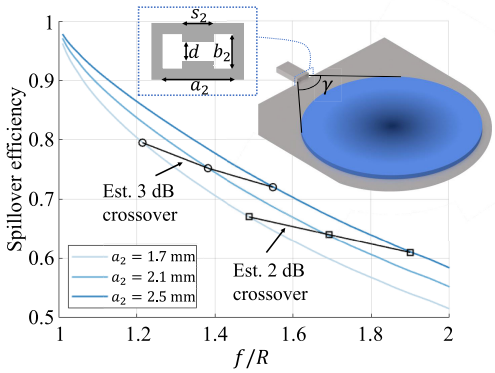

Fig. 3. Estimation of the spillover efficiency for different focal distances and feed widths. The remaining dimensions are $d = 0.35$ mm, $s_2 = 0.9$ mm, and $b_2 = 0.8$ mm.

$\pm 50°$ range. The lens is fed by ridge waveguides, which have a lower cut-off frequency than conventional rectangular waveguides for a given overall width, thus allowing further increased resolution in the feed placement.

The communication is organized as follows. In Section II, the operational principle of the geodesic generalized Luneburg lens is discussed. Furthermore, the design of the feeding network and flare, and the integration of the lens antenna are presented. In Section III, the simulation and measurement results of the lens antenna are presented. Finally, in Section IV, the conclusion of the work is presented.

II. Lens Antenna Design

The geodesic PPW lens antenna designed in this work is composed of a geodesic generalized Luneburg lens, a ridge waveguide feeding network with an antileakage structure, and an exponential flare. These components and their integration are detailed in the following.

A. Geodesic Generalized Luneburg Lens

A generalized Luneburg lens is a rotationally symmetric lens that focuses a point source at the focal point, f, to a point on the opposite side of the lens [28]. For mm-wave base station antenna applications, a lens that focuses the point source at infinity is attractive. Such a lens transforms a cylindrical wave at a radial position f to a planar wave at the diametrically opposite side of the lens. This lens can be used to produce a directive beam that can be steered in a wide angular range when integrated into an antenna.

The focal point, f, can be chosen freely, and the conventional Luneburg lens is obtained when $f = R$, where R is the lens' radius. By setting $f > R$, the focal point is moved away from the lens, and as a result, a higher resolution is obtained in the feed placement. The refractive index distribution of a generalized Luneburg lens is exemplified in Fig. 1 for the case with $f = 1.4R$. The inset depicts the ray paths when the source is placed at the radial position f. The rays are parallel at the output of the lens, indicating that a directive beam can be produced using this lens.

A rotationally symmetric gradient refractive index distribution can be mimicked using a geodesic shape [30], [31]. Fig. 2 presents the geodesic profile for the generalized Luneburg lens with $f = 1.4R$. The geodesic shape is obtained by rotating the calculated profile around the symmetry axis ($\rho = 0$). The lens is implemented in a PPW, and the calculated geodesic profile is the mean surface between the two conductors of the PPW. It is worth noting that the height of the geodesic generalized Luneburg lens is lower than that of the geodesic Luneburg lens [15] due to the reduced refractive index range in the generalized Luneburg lens. The height could be further reduced by folding the lens, as proposed in [32], or using the water drop lens concept [33]. In this work, the radius of the lens is $R = 25$ mm, which corresponds to 5 wavelengths at 60 GHz. The gap between the two PPW conductors is 0.8 mm, which is sufficiently small to ensure that only the fundamental TEM mode can propagate in the PPW. A chamfered transition is inserted between the lens and the surrounding planar PPW (at $\rho = R$) to reduce the reflections. The chamfer dimensions are $c = 0.7$ mm and $\alpha = 43°$. The inset in Fig. 2 presents the distribution of the real part of the z-component of the electric field in the shaped PPW lens excited by a point source at the focal point. We observe that the point source is transformed into a planar wave at the opposite side of the lens.

B. Feeding Network and Flare Design

The angular resolution in the feed placement is dictated by the feed radius (i.e., focal distance f) and width of the feeds. Typically, rectangular waveguides are used to feed geodesic lens antennas [15], [17]; however, their width must be larger than half-wavelength at the lowest operating frequency. A narrower feed can be designed using ridge waveguides, and therefore, ridge waveguides are used to feed the lens in this work.

When displacing the focal point from the border of the lens, part of the radiated energy from the feed does not intersect the lens, thus resulting in spillover losses. These spillover losses depend on the focal point and the radiation pattern of the feed when connected to the PPW. In Fig. 3, the spillover efficiency at 62 GHz for different ridge waveguide widths and focal points is presented. These results are obtained by simulating the ridge waveguide connected to a PPW with a gap of 0.8 mm and loaded with a dielectric planar generalized

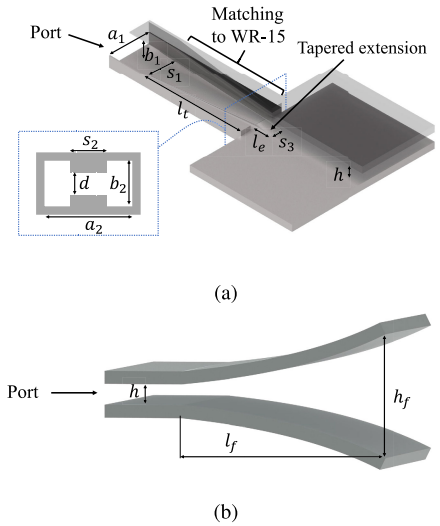

Fig. 4. (a) Simulation setup for designing the feeding waveguides. (b) Simulation setup for designing the exponential flare.

Luneburg lens with a radius $R = 25$ mm. The feed is placed at the focal point of the lens, and the simulation setup is illustrated in the inset of Fig. 3. The spillover efficiency is calculated as the ratio between the power that intersects the lens (i.e., the power within the angular region γ) and the total power radiated into the PPW. The feed dimensions are $d = 0.35$ mm, $s_2 = 0.9$ mm, and $b_2 = 0.8$ mm. We observe that a smaller feed width results in a lower spillover efficiency for a given focal radius. This is expected as a smaller feed has a less directive radiation pattern. However, smaller feeds allow for a denser feed placement and, as a result, a smaller focal distance can be used to obtain a given beam separation and crossover level.

The expected crossover level in a lens antenna implemented with an array of feeds placed along the focal curve is estimated from the radiation pattern of an aperture with the same width as the diameter of the lens with a cosine amplitude tapering. The result is presented in Fig. 3. In these calculations, the feed separation is given by the width of the waveguide and an additional 1 mm wall thickness, accounting for manufacturing constraints. In this work, we target a beam crossover gain of 3 dB below the peak gain. This crossover is chosen as a tradeoff between beam correlation (i.e., sidelobe levels and radiation efficiency [20]) and gain stability in the steering range [27]. We use a feed with a width of $a_2 = 2.1$ mm and a lens with $f/R = 1.4$. These design choices are based on a tradeoff between the ease of implementation and impedance matching of the feeding, and the spillover efficiency.

The impedance of the ridge waveguide is matched to the impedance of the PPW using a tapered extension that protrudes into the PPW. The extension has a length l_e and its width is linearly tapered from s_2 (in the aperture of the ridge waveguide) to s_3. The height of the extension is similarly tapered from $(b_2 - d)/2$ (in the aperture of the ridge waveguide) to 0. The extension is highlighted in Fig. 4(a). Standard WR-15 rectangular waveguide connectors are used for testing purposes. Therefore, a matching section between the testing waveguide and the ridge waveguide is needed. The width and height of the ridge waveguide are linearly tapered to the width and height of the testing waveguide. Simultaneously, the width and height of the ridge are tapered from $(b_2 - d)/2$ (in the aperture of the ridge waveguide) to 0. The length of the matching section is l_t, and it is highlighted in Fig. 4(a). Fig. 5 presents the reflection coefficient for the feeding waveguide when connected to a PPW with the same gap as the geodesic lens. The reflection coefficient is below -14 dB in the operational band from 57 to 67 GHz. The dimensions are indicated in the figure caption.

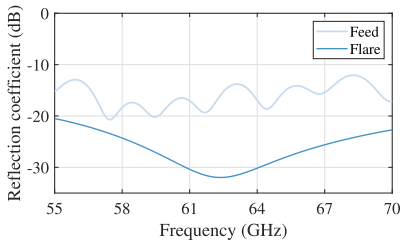

Fig. 5. Simulated reflection coefficients for the feeding waveguide and the flare. The dimensions are $a_1 = 3.8$ mm, $b_1 = 1.9$ mm, $s_1 = 1.9$ mm, $l_t = 43.3$ mm, $d = 0.35$ mm, $a_2 = 2.1$ mm, $b_2 = 0.8$ mm, $s_2 = 0.9$ mm, $l_e = 1.5$ mm, $s_3 = 1$ mm, $h = 0.8$ mm, $l_f = 10.4$ mm, and $h_f = 5$ mm.

An exponential flare is placed at the output of the lens to match the impedance of the PPW to the free-space impedance. A section of the flare is illustrated in Fig. 4(b). The dimensions of the flare are optimized through simulations of the flare section with perfect magnetic conductor boundary conditions along the lateral walls. The reflection coefficient of the flare is presented in Fig. 5, for the dimensions $h = 0.8$ mm, $l_f = 10.4$ mm, and $h_f = 5$ mm. The reflection coefficient is below -23 dB in the operational band.

C. Antileakage Structure

Geodesic lens antennas can be manufactured using conventional techniques in two parts that are joined with screws [15], [17], or in one part using additive manufacturing [34]. The feeding waveguides and flare are integrated into the same metallic blocks as the lens. We note that additive manufacturing techniques currently have sufficient tolerances for antennas at lower frequencies (up to the K_a-band [34]), but the surface roughness of additively manufactured metallic pieces introduces prohibitive losses at the V-band. Therefore, conventional milling is used to realize the antenna in two parts in this work.

In [35], it is demonstrated that the feeding structure for conventionally manufactured geodesic lenses operating at V-band frequencies is sensitive to manufacturing errors. Specifically, gaps can form between the two metallic parts in the region of the feeding waveguides. Since the waveguides are electrically long, such gaps can cause significant leakage, which translates into reduced radiation efficiency and distorted beams. The effect of these manufacturing errors can be mitigated by placing electromagnetic bandgap (EBG) structures around the feeding waveguides in critical areas [35], [36]. Here, we use a glide-symmetric holey EBG structure to improve the robustness of manufacturing tolerances [37].

The simulation setup for designing the EBG structure is illustrated in Fig. 6(a). Two parallel ridge waveguides of length L are connected through a gap of height g. Glide-symmetric EBG holes are placed in the region of the gap to reduce coupling between the waveguides. Fig. 6(b) presents the transmission coefficient through one of the waveguides for the cases of no gap, a gap of $g = 30$ μm without the EBG structure, and a gap of $g = 30$ μm with the EBG structure. The dimensions are: $L = 50$ mm, $r_H = 0.7$ mm, $p = 2.2$ mm, and $d_H = 1$ mm. We observe that leakage from the waveguide is significantly reduced using the EBG structure.

D. Integrated Lens Antenna

The integrated lens antenna is illustrated in Fig. 7. The antenna is implemented in two metallic pieces that are joined with screws. The top metallic part is partly hidden and partly transparent for increased clarity. The lens is fed by 21 waveguides with an angular separation of 5.1°, thus providing an angular coverage of 102°. The feeding

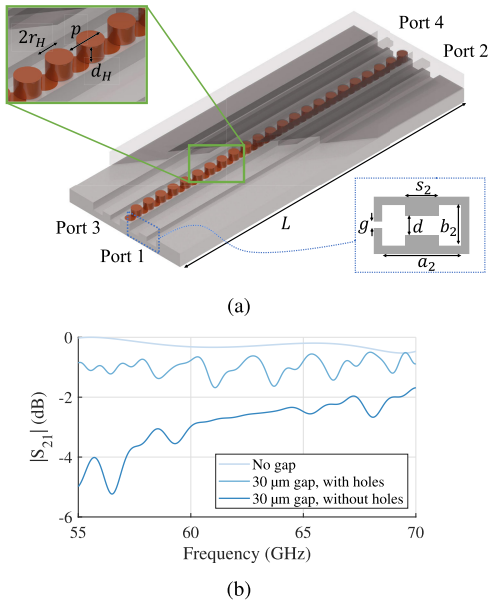

Fig. 6. (a) Simulation setup for designing the EBG structure. (b) Transmission coefficient through one waveguide for simulations with shielded waveguides, a gap between the waveguides without EBG structure, and a gap between the waveguides with EBG structure. The dimensions are: $L = 50$ mm, $r_H = 0.7$ mm, $p = 2.2$ mm, and $d_H = 1$ mm.

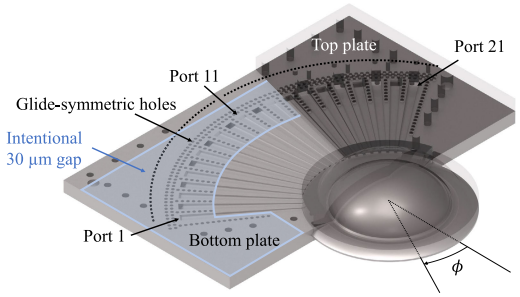

Fig. 7. Illustration of the integrated lens antenna. The top metallic plate is partly hidden and partly transparent for increased clarity.

waveguides are numbered from 1 to 21 starting and ending with the most scanned ports, as indicated in Fig. 7. The feeding waveguides are extended radially to accommodate the flanges of the standard testing waveguide. The feeding waveguides are integrated with a 90° E-plane bend to connect to the testing waveguides placed alternating in the upper and lower metallic plates. The EBG structure is placed around the waveguides to improve the robustness to manufacturing errors. Note that close to the lens, the spacing between the waveguides is too small to place the EBG structure. To improve the electrical contact in this critical region, an intentional gap of 30 μm is implemented in the region where holes can be placed [35], as indicated in Fig. 7. The prototype of the antenna is presented in Fig. 8.

III. Results

The antenna is simulated in the *time-domain solver* of *CST*. The simulation results are experimentally validated using an Anritsu MS4647B VNA and the anechoic chamber at KTH. Fig. 9(a) presents the simulated and measured reflection coefficients for ports 1–11. In the measurements, the effects of the connecting testing waveguides have been removed using time-gating. The simulated and measured reflection coefficients are below −15 and −10 dB, respectively, in the operational band. Fig. 9(b) presents the simulated and measured coupling coefficients for selected ports. The reported cases are

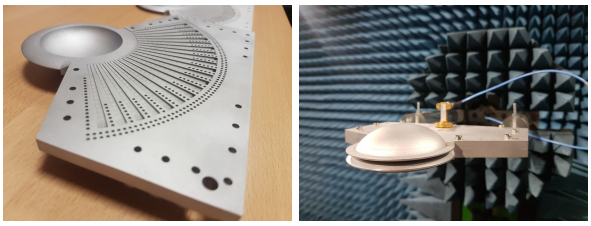

Fig. 8. (a) Photograph of the prototype. (b) Measurement setup in the anechoic chamber.

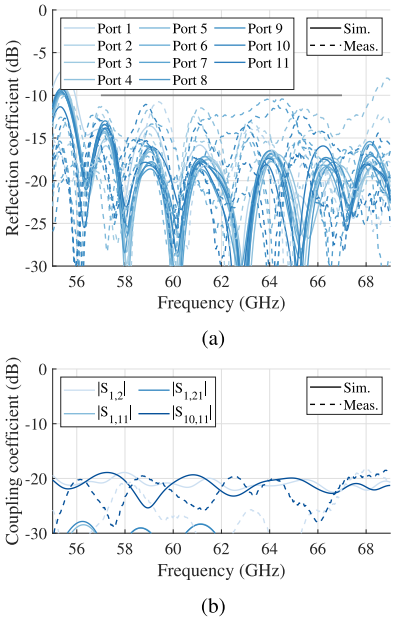

Fig. 9. (a) Simulated and measured reflection coefficients for ports 1–11. The remaining ports are symmetric to these ports. (b) Simulated and measured selected coupling coefficients.

expected to include the most significant coupling coefficients, and we observe that the coupling is below roughly −20 dB in the operational band.

Fig. 10 presents the simulated and measured normalized H-plane radiation patterns at 57, 62, and 67 GHz. The gray lines correspond to the symmetric ports to ports 1–10. The measured sidelobe levels are below −10 dB for all ports and frequencies and the steering range is roughly 100°. We note that the E-plane radiation pattern is wide due to the limited aperture size in that direction. The directivity in the E-plane can be increased by stacking multiple lenses, as proposed in [9] and [36], which also allows for beamsteering in the E-plane. Fig. 11 presents the simulated directivity and the simulated and measured peak realized gain for ports 1–11. We observe that the peak realized gain varies by less than 1 dB at each frequency throughout the steering range. Furthermore, we note that the simulated radiation efficiency is roughly 85% in the operation band and that the ohmic losses are more significant than other loss sources. The lower gain in the measurements compared to simulations is attributed to additional ohmic losses caused by the surface roughness in the manufactured prototype. The surface roughness is estimated to be around 2–3 μm (rms), and simulations including 3-μm surface roughness are in good agreement with the measurements, as demonstrated in Fig. 11. These losses can be reduced with a smooth surface in important regions of the device, for instance, obtained through polishing.

Fig. 12 presents the normalized radiation pattern envelope in the H-plane of the antenna at 57, 62, and 67 GHz. The envelopes are normalized to the peak at each frequency, and simulations and

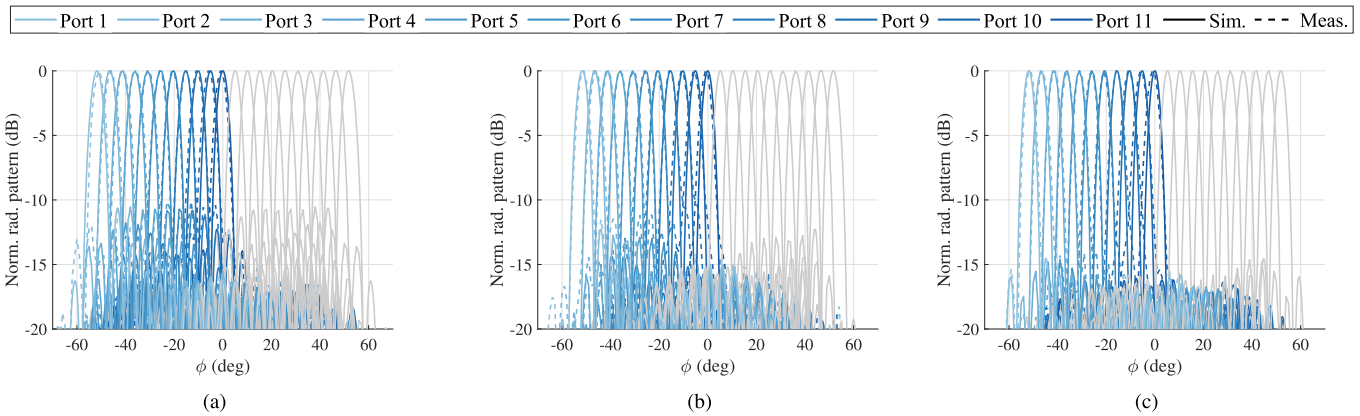

Fig. 10. Simulated and measured normalized radiation patterns in the H-plane at (a) 57, (b) 62, and (c) 67 GHz. The gray lines correspond to the symmetric ports and demonstrate the wide steering range of the antenna.

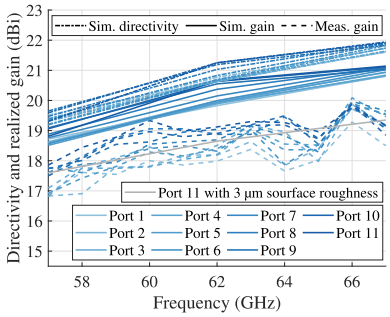

Fig. 11. Simulated directivity and simulated and measured peak realized gains. A simulation of the gain of port 11 with 3-μm surface roughness in the metallic parts is included.

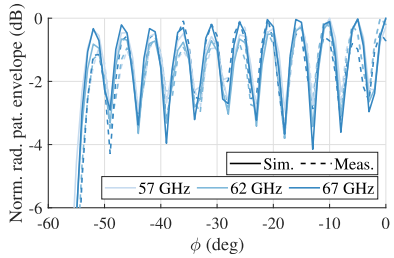

Fig. 12. Simulated and measured normalized radiation pattern envelopes. The envelopes are normalized to the peak at each frequency, and simulations and measurements are normalized independently.

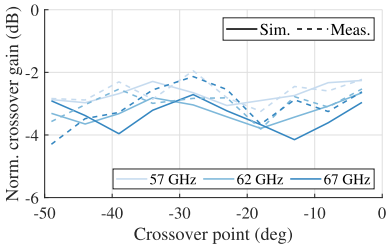

Fig. 13. Simulated and measured crossover gain normalized to the peak gain at each frequency. The simulations and measurements are normalized independently.

TABLE I
COMPARISON OF GEODESIC ROTATIONALLY SYMMETRIC LENS ANTENNAS

Ref.	Frequency	Sim. aperture efficiency	Crossover gain below peak gain	In-band side lobe level
[15]	28-36 GHz	$\approx$85%	6-8 dB	-19 to -16 dB
[17]	26-32 GHz	$\approx$85%	6-10 dB	$\approx$-15 dB
[26]	30-35 GHz	$\approx$30%	2-3 dB	$\approx$-15 dB
[35]	56-62 GHz	$\approx$85%	6-8 dB	-15 to -13 dB
[38]	25-31 GHz	$\approx$85%	6-7 dB	$\approx$-15 dB
This work	57-67 GHz	$\approx$90%	2-4 dB	-15 to -10 dB

measurements are normalized independently. We observe that the gain varies by less than 4 dB at each frequency throughout the scanning range. The gain at the crossover points is represented in Fig. 13. The crossover gain between adjacent beams is 2–4 dB lower than the peak gain for all frequencies, in both measurements and simulations.

Table I compares the performance of reported fully-metallic geodesic rotationally symmetric lens antennas. The crossover in this work is significantly higher than in reported geodesic Luneburg lens antennas [15], [17], [35], [38]. The crossover gain in the presented antenna is slightly lower than that of the antenna in [26]. However, the simulated aperture efficiency (calculated by comparing the simulated directivity of the antenna with that of a uniformly illuminated rectangular aperture with sides given by the diameter of the lens and the height of the flare) is significantly higher in the proposed antenna. The simulated radiation efficiency is roughly 85%, which is similar to the radiation efficiency of a conventional geodesic Luneburg lens antenna operating at the same frequency [35], indicating a low beam correlation in the presented antenna. The sidelobe level of the proposed antenna is slightly higher compared to the other geodesic lens antennas. The higher level stems from an increased crossover level and a more uniform amplitude distribution in the aperture, resulting from the feed element radiation pattern and placement.

IV. CONCLUSION

In this work, we demonstrate that a generalized Luneburg lens can be used to increase the beam crossover gain when integrated into an antenna compared to the reported conventional Luneburg lens antennas. The high crossover gain is a consequence of the high angular resolution in the feed placement, which is achieved by displacing the focal curve from the lens. We design a geodesic generalized Luneburg lens antenna operating at the V-band (from 57 to 67 GHz). The lens is fed by 21 ridge waveguides with an angular separation of 5.1°, and the antenna produces a directive beam in a 102° steering

range. The crossover gain is between 2 and 4 dB below the peak gain for all steering directions and frequencies. This is significantly higher than previously reported conventional Luneburg lens antennas, where the crossover gain is typically between 6 and 10 dB below the peak gain. The simulated peak realized gain is between 19 and 21 dBi, and the simulated radiation efficiency is roughly 85%, for all steering angles in the operational band. The measured peak realized gain is roughly 1–2.5 dB lower than the simulated gain for all steering angles in the operational band. This gain reduction is attributed to increased ohmic losses due to surface roughness in the manufactured prototype. The antenna is intended for base stations in future mm-wave communication systems, where a stable gain over a wide coverage is required to ensure optimal service to all end users.

REFERENCES

[1] G. Sellin. (Oct. 2022). *Ericsson Microwave Outlook*. Accessed: Oct. 27, 2022. [Online]. Available: https://www.ericsson.com/en/reports-and-papers/microwave-outlook

[2] Y. J. Guo, M. Ansari, R. W. Ziolkowski, and N. J. G. Fonseca, "Quasi-optical multi-beam antenna technologies for B5G and 6G mmWave and THz networks: A review," *IEEE Open J. Antennas Propag.*, vol. 2, pp. 807–830, 2021.

[3] M. Ettorre, R. Sauleau, and L. Le Coq, "Multi-beam multi-layer leaky-wave SIW pillbox antenna for millimeter-wave applications," *IEEE Trans. Antennas Propag.*, vol. 59, no. 4, pp. 1093–1100, Apr. 2011.

[4] M. Ettorre, F. F. Manzillo, M. Casaletti, R. Sauleau, L. L. Coq, and N. Capet, "Continuous transverse stub array for Ka-band applications," *IEEE Trans. Antennas Propag.*, vol. 63, no. 11, pp. 4792–4800, Nov. 2015.

[5] Y. J. Cheng et al., "Substrate integrated waveguide (SIW) Rotman lens and its Ka-band multibeam array antenna applications," *IEEE Trans. Antennas Propag.*, vol. 56, no. 8, pp. 2504–2513, Aug. 2008.

[6] W. Lee, J. Kim, and Y. J. Yoon, "Compact two-layer Rotman lens-fed microstrip antenna array at 24 GHz," *IEEE Trans. Antennas Propag.*, vol. 59, no. 2, pp. 460–466, Feb. 2011.

[7] F. Doucet et al., "Shaped continuous parallel plate delay lens with enhanced scanning performance," *IEEE Trans. Antennas Propag.*, vol. 67, no. 11, pp. 6695–6704, Nov. 2019.

[8] H. B. Molina, J. G. Marin, and J. Hesselbarth, "Modified planar Luneburg lens millimetre-wave antenna for wide-angle beam scan having feed locations on a straight line," *IET Microw., Antennas Propag.*, vol. 11, no. 10, pp. 1462–1468, Jul. 2017.

[9] J. G. Marin and J. Hesselbarth, "Lens antenna with planar focal surface for wide-angle beam-steering application," *IEEE Trans. Antennas Propag.*, vol. 67, no. 4, pp. 2757–2762, Apr. 2019.

[10] C. Z. Hua, X. D. Wu, N. Yang, and W. Wu, "Millimeter-wave homogenous cylindrical lens antenna for multiple fan-beam scanning," *J. Electromagn. Waves Appl.*, vol. 26, nos. 14–15, pp. 1922–1929, Sep. 2012.

[11] O. Manoochehri, A. Darvazehban, M. A. Salari, A. Emadeddin, and D. Erricolo, "A parallel plate ultrawideband multibeam microwave lens antenna," *IEEE Trans. Antennas Propag.*, vol. 66, no. 9, pp. 4878–4883, Sep. 2018.

[12] R. K. Luneburg, *Mathematical Theory of Optics*. Providence, RI, USA: Brown Univ. Press, 1944.

[13] C. Pfeiffer and A. Grbic, "A printed, broadband Luneburg lens antenna," *IEEE Trans. Antennas Propag.*, vol. 58, no. 9, pp. 3055–3059, Sep. 2010.

[14] M. K. Saleem, H. Vettikaladi, M. A. S. Alkanhal, and M. Himdi, "Lens antenna for wide angle beam scanning at 79 GHz for automotive short range radar applications," *IEEE Trans. Antennas Propag.*, vol. 65, no. 4, pp. 2041–2046, Apr. 2017.

[15] Q. Liao, N. J. G. Fonseca, and O. Quevedo-Teruel, "Compact multibeam fully metallic geodesic Luneburg lens antenna based on non-Euclidean transformation optics," *IEEE Trans. Antennas Propag.*, vol. 66, no. 12, pp. 7383–7388, Dec. 2018.

[16] H. Lu, Z. Liu, Y. Liu, H. Ni, and X. Lv, "Compact air-filled Luneburg lens antennas based on almost-parallel plate waveguide loaded with equal-sized metallic posts," *IEEE Trans. Antennas Propag.*, vol. 67, no. 11, pp. 6829–6838, Nov. 2019.

[17] N. J. G. Fonseca, Q. Liao, and O. Quevedo-Teruel, "Equivalent planar lens ray-tracing model to design modulated geodesic lenses using non-Euclidean transformation optics," *IEEE Trans. Antennas Propag.*, vol. 68, no. 5, pp. 3410–3422, May 2020.

[18] M. Ettorre and R. Sauleau, "Reconfigurable multi-beam pillbox antenna for millimeter wave automotive radars," in *Proc. 9th Int. Conf. Intell. Transp. Syst. Telecommun., (ITST)*, Oct. 2009, pp. 87–90.

[19] W. White, "Pattern limitations in multiple-beam antennas," *IRE Trans. Antennas Propag.*, vol. 10, no. 4, pp. 430–436, Jul. 1962.

[20] S. Stein, "On cross coupling in multiple-beam antennas," *IRE Trans. Antennas Propag.*, vol. 10, no. 5, pp. 548–557, Sep. 1962.

[21] K. Tekkouk, M. Ettorre, E. Gandini, and R. Sauleau, "Multibeam pillbox antenna with low sidelobe level and high-beam crossover in SIW technology using the split aperture decoupling method," *IEEE Trans. Antennas Propag.*, vol. 63, no. 11, pp. 5209–5215, Nov. 2015.

[22] F. F. Manzillo et al., "A wide-angle scanning switched-beam antenna system in LTCC technology with high beam crossing levels for V-band communications," *IEEE Trans. Antennas Propag.*, vol. 67, no. 1, pp. 541–553, Jan. 2019.

[23] X. Lu, S. Gu, X. Wang, H. Liu, and W. Lu, "Beam-scanning continuous transverse stub antenna fed by a ridged waveguide slot array," *IEEE Antennas Wireless Propag. Lett.*, vol. 16, pp. 1675–1678, 2017.

[24] T. Ströber, S. Tubau, E. Girard, H. Legay, G. Goussetis, and M. Ettorre, "Shaped parallel-plate lens for mechanical wide-angle beam steering," *IEEE Trans. Antennas Propag.*, vol. 69, no. 12, pp. 8158–8169, Dec. 2021.

[25] H.-T. Chou, Y.-S. Chang, H.-J. Huang, Z.-D. Yan, T. Lertwiriyaprapa, and D. Torrungrueng, "Two-dimensional multi-ring dielectric lens antenna to radiate fan-shaped multi-beams with optimum adjacent-beam overlapping crossover by genetic algorithm," *IEEE Access*, vol. 8, pp. 79124–79133, 2020.

[26] O. Orgeira, G. León, N. J. G. Fonseca, P. Mongelos, and O. Quevedo-Teruel, "Near-field focusing multibeam geodesic lens antenna for stable aggregate gain in far-field," *IEEE Trans. Antennas Propag.*, vol. 70, no. 5, pp. 3320–3328, May 2022.

[27] A. Algaba-Brazález et al., "Crossover level improvement between beams in a geodesic lens antenna based on a generalized Luneburg lens," in *Proc. 16th Eur. Conf. Antennas Propag. (EuCAP)*, Mar. 2022, pp. 1–5.

[28] S. P. Morgan, "General solution of the Luneberg lens problem," *J. Appl. Phys.*, vol. 29, no. 9, pp. 1358–1368, Sep. 1958.

[29] C. Liang, J. Dorsey, J. Johnston, and W. Zant, "The design of generalized Luneberg geodesic lenses," in *Proc. Antennas Propag. Soc. Int. Symp.*, vol. 9, 1971, pp. 220–223.

[30] R. F. Rinehart, "A solution of the problem of rapid scanning for radar antennae," *J. Appl. Phys.*, vol. 19, no. 9, pp. 860–862, Sep. 1948.

[31] R. Rinehart, "A family of designs for rapid scanning radar antennas," *Proc. IRE*, vol. 40, no. 6, pp. 686–688, Jun. 1952.

[32] K. S. Kunz, "Propagation of microwaves between a parallel pair of doubly curved conducting surfaces," *J. Appl. Phys.*, vol. 25, no. 5, pp. 642–653, May 1954.

[33] O. Quevedo-Teruel et al., "Geodesic lens antennas for 5G and beyond," *IEEE Commun. Mag.*, vol. 60, no. 1, pp. 40–45, Jan. 2022.

[34] J. Rico-Fernández, F. V. Vidarsson, N. J. G. Fonseca, and O. Quevedo-Teruel, "Compact and lightweight additive manufactured parallel-plate waveguide half-Luneburg geodesic lens multiple-beam antenna in the K_a-band," *IEEE Antennas Wireless Propag. Lett.*, vol. 22, no. 4, pp. 684–688, Apr. 2023.

[35] O. Zetterstrom, M. Petek, P. Castillo-Tapia, A. Palomares-Caballero, N. J. G. Fonseca, and O. Quevedo-Teruel, "V-band fully metallic geodesic Luneburg lens antenna," *IEEE Trans. Antennas Propag.*, vol. 71, no. 2, pp. 1965–1970, Feb. 2023.

[36] P. Castillo-Tapia et al., "Two-dimensional beam steering using a stacked modulated geodesic Luneburg lens array antenna for 5G and beyond," *IEEE Trans. Antennas Propag.*, vol. 71, no. 1, pp. 487–496, Jan. 2023.

[37] M. Ebrahimpouri, E. Rajo-Iglesias, Z. Sipus, and O. Quevedo-Teruel, "Cost-effective gap waveguide technology based on glide-symmetric holey EBG structures," *IEEE Trans. Microw. Theory Techn.*, vol. 66, no. 2, pp. 927–934, Feb. 2018.

[38] F. V. Vidarsson et al., "Conformal parallel plate waveguide polarizer integrated in a geodesic lens antenna," *IEEE Trans. Antennas Propag.*, vol. 70, no. 11, pp. 10327–10337, Nov. 2022.